Li-Ion Batteries

Confined Nanospace Pyrolysis for the Fabrication of Coaxial Fe_3O_4@C Hollow Particles with a Penetrated Mesochannel as a Superior Anode for Li-Ion Batteries

Cheng Lei, Fei Han, Qiang Sun, Wen-Cui Li, and An-Hui Lu*[a]

Abstract: In this study, a method is developed to fabricate Fe_3O_4@C particles with a coaxial and penetrated hollow mesochannel based on the concept of "confined nanospace pyrolysis". The synthesis involves the production of a polydopamine coating followed by a silica coating on a rod-shaped β-FeOOH nanoparticle, and subsequent treatment by using confined nanospace pyrolysis and silica removal procedures. Typical coaxial hollow Fe_3O_4@C possesses a rice-grain morphology and mesoporous structure with a large specific surface area, as well as a continuous and flexible carbon shell. Electrochemical tests reveal that the hollow Fe_3O_4@C with an open-ended nanostructure delivers a high specific capacity (ca. 864 mA h g^{-1} at 1 A g^{-1}), excellent rate capability with a capacity of about 582 mA h g^{-1} at 2 A g^{-1}, and a high Coulombic efficiency (>97%). The excellent electrochemical performance benefits from the hollow cavity with an inner diameter of 18 nm and a flexible carbon shell that can accommodate the volume change of the Fe_3O_4 during the lithium insertion/extraction processes as well as the large specific surface area and open inner cavity to facilitate the rapid diffusion of lithium ions from electrolyte to active material. This fabrication strategy can be used to generate a hollow or porous metal oxide structure for high-performance Li-ion batteries.

Introduction

The ever-growing demand for high-performance power sources has prompted tremendous research effort towards the development of new anode materials with improved power density per unit mass (gravimetric capacity) for the next generation of lithium-ion batteries (LIBs).[1–4] Fe_3O_4-based nanostructured materials are attracting growing attention as high-capacity anode electrodes for LIBs due to their high theoretical capacity (ca. 928 mA h g^{-1}, which is about 3 times that of conventional graphite), low cost, low toxicity, eco-friendliness, and the natural abundance of iron.[5–10] However, their practical application is still hindered by poor cyclic performance and rate capability, resulting from their intrinsically low electronic conductivity, sluggish ion diffusion ability, and severe aggregation of nanoparticles during cycling.[11–13] Moreover, the large volume change (ca. 200%) of Fe_3O_4 that occurs upon Li^+ insertion and extraction causes mechanical degradation, which hastens the loss of capacity.[14,15] To mitigate the problem of aggregation and increase the electronic conductivity of nanosized Fe_3O_4, carbon coatings have been extensively explored.[16–18] Carbon-coated Fe_3O_4 nanorods,[19] nanospindles,[6] and nanowires[20,21] have been synthesized and have shown better electrochemical performance than the corresponding pure Fe_3O_4 electrode. However, the carbon coating applied on nonporous particles thus far has two drawbacks. First, a compact carbon coating layer cannot allow residual buffer space to relieve the stress arising from the large volume changes during Li^+ insertion and extraction. This results in the capacity fading in the case of a large charge current.[22,23] Second, the carbon coating on the nonporous particles did not improve the active material/electrolyte contact area, leading to inefficient electron and ion diffusion inside the particles and a consequent poor rate capacity.

The fabrication of hollow and/or porous nanostructures with a relatively large specific surface area and pore volume is another useful strategy for improving the electrochemical performance of an oxide anode material.[24–29] The pores can buffer the volume change to some extent, while increasing the active material/electrolyte interface area and shortening the electron and ion transport distance.[4] In view of the limited improvement in the electrochemical performance of these two strategies alone, we have attempted to simultaneously fabricate a hollow/penetrated mesochannel structure and carbon coating in a single Fe_3O_4-based hybrid material in the hope that it will significantly improve the electrochemical performance.

Herein, we describe a new method, referred to as "confined nanospace pyrolysis", for preparing coaxial Fe_3O_4@C hollow particles with a rice-grain morphology, penetrated mesochannel, and a continuous carbon shell. When evaluated for its lithium storage capability, the anode composed of this material

[a] C. Lei, F. Han, Q. Sun, Prof. Dr. W.-C. Li, Prof. Dr. A.-H. Lu
State Key Laboratory of Fine Chemicals
School of Chemical Engineering
Dalian University of Technology
Dalian 116024 (P.R. China)
Fax: (+86) 411-84986112
E-mail: anhuilu@dlut.edu.cn

Supporting information for this article is available on the WWW under http://dx.doi.org/10.1002/chem.201303175.

shows excellent cycling performance and charge-rate capability, accompanied by high Coulombic efficiency.

Results and Discussion

Figure 1 illustrates the fabrication process of the coaxial Fe_3O_4@C hollow particles. First, rod-shaped akagenite (β-FeOOH) nanoparticles were obtained from the hydrolysis of an aqueous iron chloride solution ($FeCl_3 \cdot 6H_2O$),[30] then the surface of the akagenite was coated with polydopamine by immersion in a aqueous solution of dopamine (pH ≈ 8.5) in the presence of oxygen. This coating method has been reported to give a highly uniform polydopamine coating layer with a thickness that can be controlled by varying the coating time and dopamine concentration.[31–33] Subsequently, the outer surface of the β-FeOOH@polydopamine was coated with a layer of silica by a modified Stöber method. When confined by both the polymer and silica shells, the akagenite core of β-FeOOH@polydopamine@SiO_2 can be converted into a Fe_3O_4 hollow particle by thermal treatment as a result of the combined thermal dehydroxylation of the FeOOH, and internal pressure forced core expansion. Meanwhile, the polydopamine layer transforms into a uniform and continuous N-doped carbon layer, resulting in the formation of hollow Fe_3O_4@C@SiO_2 nanoparticles. In this case, the silica shell not only prevents the aggregation of the Fe_3O_4@C nanoparticles, but also causes the pores formed to join together and induces the reinforcement of pressure in the core as a result of the confined environment, thus generating hollow double-walled particles. Coaxial Fe_3O_4@C hollow particles were obtained after removal of the silica by an alkaline solution. To obtain insight into the development of the hollow structure and monitor the internal structural changes during the heat treatment, the β-FeOOH precursor has been treated and pyrolyzed in different microenvironments. For example, pyrolysis of pure β-FeOOH, β-FeOOH@SiO_2, and β-FeOOH@polydopamine resulted in the formation of Fe_2O_3 particles, porous Fe_3O_4 (P-Fe_3O_4), and a porous Fe_3O_4@C hybrid material (P-Fe_3O_4@C), respectively. The preparation procedures are illustrated in Figure S1 in the Supporting Information. In particular, to further test the structural stability of the hollow Fe_3O_4 particles and to prove the vital function of the carbon shells of the Fe_3O_4@C hollow particles in improving the electrochemical performance, we made hollow Fe_3O_4 rods (H-Fe_3O_4) out of the hollow Fe_3O_4@C@SiO_2 by using combustion, hydrogen reduction, and silica removal procedures.

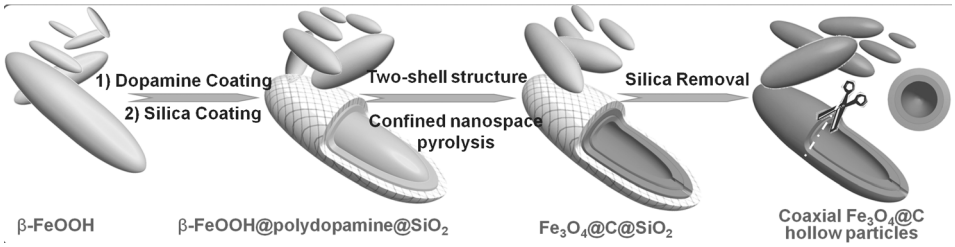

Figure 1. Illustration of the fabrication procedure for coaxial Fe_3O_4@C hollow particles with a penetrated mesochannel.

Figure 2a shows the transmission electron microscope (TEM) images of the as-synthesized β-FeOOH nanoparticles, which are rod shaped with a central diameter of approximately 70 nm and a length of about 300 nm. Figure 2b shows the TEM image of polydopamine-coated β-FeOOH nanoparticles in

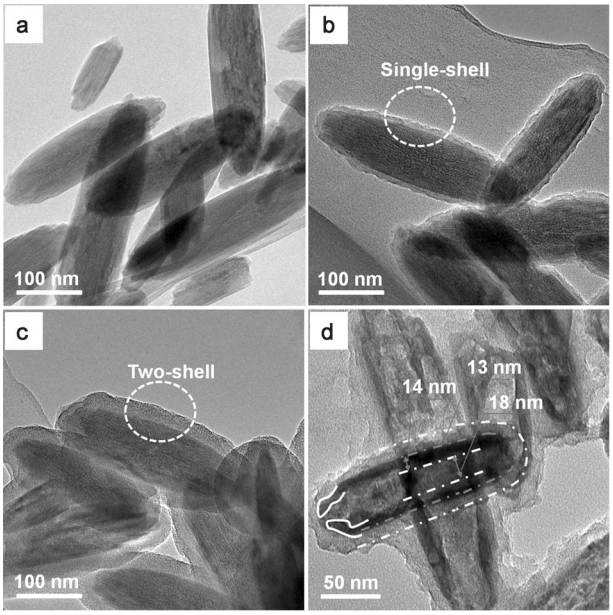

Figure 2. TEM images of a) as-synthesized β-FeOOH, b) β-FeOOH@polydopamine, c) β-FeOOH@polydopamine@SiO_2, and d) coaxial Fe_3O_4@C hollow particles.

which the outer shell and the β-FeOOH core are visible. The polydopamine coating did not change the morphology of the β-FeOOH, indicating a conformal and uniform coating of polydopamine on the akagenite surface. In Figure 2c, the TEM image of β-FeOOH@polydopamine@SiO_2 particles shows that the total thickness of the two polydopamine and silica shells is about 45 ± 5 nm, which is almost twice as thick as that of a single polydopamine layer. The TEM images clearly show that we have fabricated a material with an iron oxide core and two shells. After pyrolysis and removal of silica, the coaxial Fe_3O_4@C hollow particles with a continuous carbon coating and an interior cavity have been authenticated by use of TEM (Figure 2d). This indicates that during pyrolysis the solid iron oxide core became almost entirely hollow and the polydopamine converted into a uniform and continuous carbon layer. The corresponding SEM images of the products have further proven their structural features (Figure S2 in the Supporting Information). By comparing the structures resulting from the samples (Fe_2O_3 particles, P-Fe_3O_4, and P-Fe_3O_4@C, Figure S3 a,b,c in the Supporting Information) that do not have a hollow structure, one can deduce that the two-shell structure plays a crucial role in gen-

erating the hollow structure during pyrolysis. With only a silica or polydopamine shell, it is impossible to achieve a perfectly hollow structure despite the presence of pores in the samples. As a control, direct pyrolysis of β-FeOOH nanoparticles at 500 °C under nitrogen resulted in the formation of rhombic particles, a major shape change. This again confirmed the importance of the confinement in guiding the structure evolution. The TEM image (Figure S3 d in the Supporting Information) of H-Fe_3O_4, which was prepared through burning away the carbon shell of the hollow Fe_3O_4@C@SiO_2 particles, followed by hydrogen reduction and silica removal procedures, strongly confirms that the hollow structure of the coaxial Fe_3O_4@C hollow particles is nicely formed and structurally stable.

As seen from the TEM image in Figure 2 d, the internal core diameter is estimated to be approximately 18.0 nm and the thicknesses of the carbon shell and the magnetite nanocapsule are estimated to be approximately 13.0 and 14.0 nm, respectively. It is interesting to note that there are small holes (Figure 3 a,b) with diameters of a few nanometers at the ends of the coaxial Fe_3O_4@C hollow particles, which were presumably created during thermal dehydroxylation and pyrolysis. Such openings and hollow structures may also facilitate the Li-ion diffusion and easily allow contact with the iron oxide core, resulting in improved electrochemical performance.[34] The HRTEM image in Figure 3 c shows that the lattice fringe spacing for Fe_3O_4 is around 0.25 nm, which agrees well with the interplanar spacing of the (311) planes.[35] It is important to note that the hollow Fe_3O_4 particle is firmly attached to the carbon shell. Combining the hollow interior space and an elastic buffering carbon shell, such a "breathable" structure is anticipated to offer great promise for improving the electrochemical performance of Fe_3O_4-based anodes.[4,36]

Figure 4 a shows the powder X-ray diffraction (XRD) pattern of the hydrolyzed product, in which all peaks are in good agreement with β-FeOOH (JCPDS no.75-1594). In contrast, the diffraction peaks of coaxial Fe_3O_4@C hollow particles are similar to that of pure Fe_3O_4 (JCPDS no.65-3107), indicating that the akagenite particles have been transformed onto the face-centered cubic phase of magnetite during the pyrolysis. The XRD pattern of the coaxial Fe_3O_4@C hollow particles lacks peaks corresponding to graphite, indicating that the carbon layer is amorphous. By using the Scherrer formula, the average crystallite sizes of β-FeOOH and the coaxial Fe_3O_4@C hollow particles were calculated to be approximately 72 and 14 nm, corresponding to the initial central diameter of the as-synthesized β-FeOOH and thin walls of the resulting particles. This reveals that the confinement effect forces the formation of the hollow structure rather than the agglomeration of Fe_3O_4 during the volume change of the transition from β-FeOOH to magnetite. As shown in Figure 4 b, the weight loss of the coaxial Fe_3O_4@C hollow particle

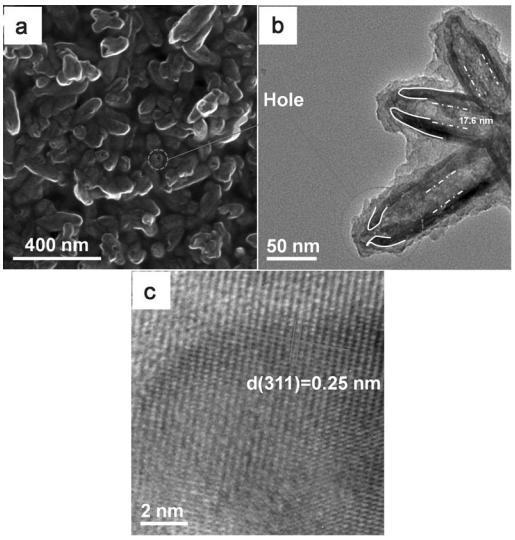

Figure 3. a) SEM b) TEM, and c) high-magnification TEM images of coaxial Fe_3O_4@C hollow particles. The central arrow in b) indicates a length of 17.6 nm.

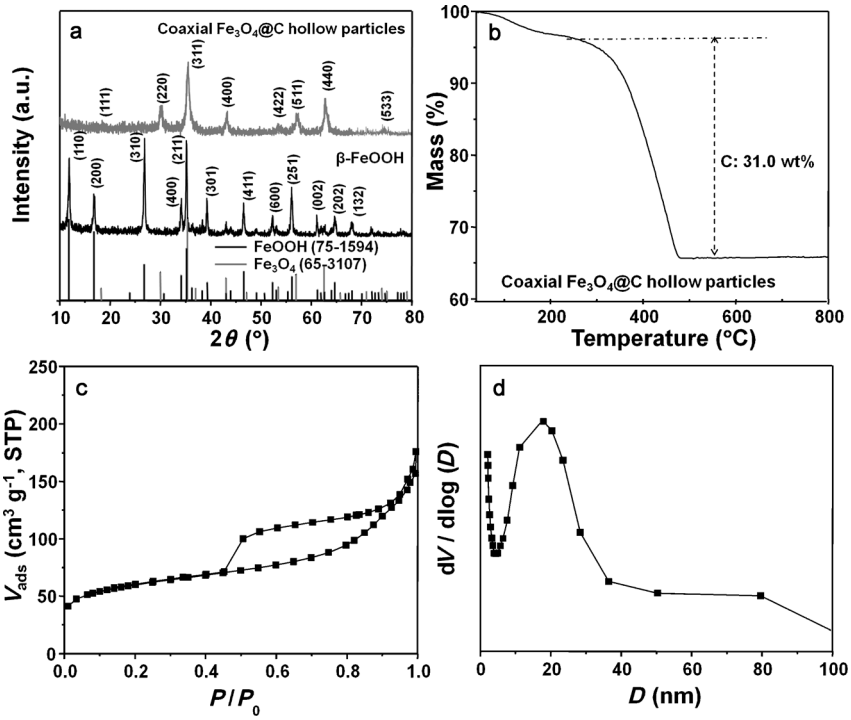

Figure 4. a) XRD patterns of coaxial Fe_3O_4@C particles and rod-shaped β-FeOOH, and b) TG curve, c) N_2 sorption isotherm, and d) the corresponding pore size distribution (PSD) of coaxial Fe_3O_4@C hollow particles. STP indicates standard temperature and pressure.

below 200 °C is attributed to the evaporation of the adsorbed moisture or gas molecules, and the major weight loss takes place between 300 and 450 °C, giving rise to an observed weight loss of 31.0 wt %.

The surface areas of the Fe_2O_3 particles, P-Fe_3O_4, P-Fe_3O_4@C, coaxial Fe_3O_4@C hollow particles, and H-Fe_3O_4 were determined by nitrogen sorption measurements at 77.4 K, and the results are shown in Figure 4c and Figure S4 in the Supporting Information. As shown in Figure 4c, the nitrogen sorption isotherm of the coaxial Fe_3O_4@C hollow particles is type IV, with a distinct hysteresis loop in the relative pressure range of 0.45–0.9, suggesting a mesoporous structure.[37,38] It is clear that the increase in the specific surface area is mainly attributed to the formation of the hollow cavity. The BET surface area and the total pore volume are determined to be 209.5 $m^2 g^{-1}$ and 0.20 $cm^3 g^{-1}$, respectively. The pore-size distribution (Figure 4d) obtained from the adsorption branch by using the Barrett–Joyner–Halenda method is mainly centered at approximately 18 nm, which agrees well with the sizes of the hollow cavity of Fe_3O_4 observed in the TEM images. Note that our coaxial Fe_3O_4@C hollow particles show a much larger specific surface area and total pore volume than previously reported iron-based hybrid materials (for a detailed comparison, see Table S1 in the Supporting Information). As shown in Table 1, the coaxial Fe_3O_4@C hollow particles obtained from the two-shell structure have a well-developed pore structure compared to the samples from the single-shell structure, for example, the polydopamine shell (sample P-Fe_3O_4@C) or silica shell (sample P-Fe_3O_4). In the ternary hybrid material of β-FeOOH@polydopamine@SiO_2, the polydopamine and silica shells can create a confined environment, in which the gas molecules (CO, H_2O, H_2, etc.), arising from the dehydration of β-FeOOH and the pyrolysis of the polydopamine shell, will preferentially diffuse inward and generate a large pressure. The internal pressure is beneficial to the cavity formation and development, which agrees with previous work.[39,40] Consequently, the specific surface area and hollow core space increased substantially. Although there are some porous characteristics in the resulting samples of P-Fe_3O_4@C and P-Fe_3O_4, which have been shown in the TEM images and N_2 sorption isotherms (Figures S3 and S4 in the Supporting Information), the specific surface area and pore structure are inferior to that of the coaxial Fe_3O_4@C hollow particles. These results evidently reveal that the "two-shell layer" plays a crucial role in the hollow cavity development. To further verify this, we reduced the polydopamine content in the β-FeOOH@polydopamine@SiO_2 material by changing the initial dopamine concentration from 1 to 0.25 mg mL^{-1}. As expected, the structure parameters (Figure S5 in the Supporting Information) of the resulting sample with a carbon content of 13.9 wt % are superior to P-Fe_3O_4, but inferior to coaxial Fe_3O_4@C hollow particles. This again confirms the important function of the polydopamine shell in determining the evolution of the structure of the hybrid material.

Table 1. Structural parameters of Fe_2O_3 particles, P-Fe_3O_4, P-Fe_3O_4@C, H-Fe_3O_4, and coaxial Fe_3O_4@C hollow particles.

Sample name	S_{BET}[a] [$m^2 g^{-1}$]	V_{total}[b] [$cm^3 g^{-1}$]	V_{mic}[c] [$cm^3 g^{-1}$]
Fe_2O_3 particles	3.2	–	–
P-Fe_3O_4	105.4	0.14	–
P-Fe_3O_4@C	174.2	0.12	0.03
coaxial Fe_3O_4@C hollow particles	209.5	0.20	0.04
H-Fe_3O_4	219.2	0.20	0.04

[a] S_{BET} = the specific surface areas calculated from the adsorption data in the relative pressure range of 0.05 to 0.3 by using the Brunauer–Emmett–Teller (BET) method. [b] V_{total} = the total pore volume at $P/P_0 = 0.90$. [c] V_{mic} = the micropore volume calculated by the t-plot method.

Because of the excellent physical properties (e.g., high surface area, hollow interior, thin shell, and continuous carbon coating) of the coaxial Fe_3O_4@C hollow particles, they may allow good contact between the electrolyte and the active materials, and shorten the transport channels for ions and electrons. We thus investigated the use of the material as an anode for LIBs. Coin2025-type cells of Fe_3O_4@C particles, by using carbon black as an additional conductive additive, against a lithium-metal counter electrode were assembled and subjected to cyclic voltammetry (CV) experiments (Figure 5a), followed by galvanostatic charge–discharge cycling (Figure 5b). As shown, the doublet (first sweep) located around 0.27 V with a shoulder at about 0.6 V can be attributed to the formation of Li_2O, as well as a solid electrolyte interface (SEI) film and the decomposition of the electrolyte. The subsequent well-defined anodic peak at 1.9 V indicates the extraction of Li from the electrode material. These results coincide with the voltage plateaus in the galvanostatic discharge–charge curves (Figure 5b). The second cathodic sweep differs slightly from the first one, indicating different redox behavior. It is worth noting that the CV peaks overlap well during subsequent cycles. This means that the electrochemical reaction becomes highly reversible after the first discharge–charge cycle. It appears that the lithium storage mechanism of the coaxial Fe_3O_4@C hollow particles is similar to that of other iron oxide based electrodes.[41–44] However, benefitting from the tightly connected conductive N-doped carbon layer on the iron oxide, coaxial Fe_3O_4@C hollow particles exhibit much lower resistance than H-Fe_3O_4 and Fe_2O_3 particles, as shown by the drastically reduced diameter of the semicircle in the high-frequency region and the appreciably steep slope of the line in the graph (Figure S6 in the Supporting Information).

Figure 5b depicts the discharge–charge voltage profiles of the coaxial Fe_3O_4@C hollow particles for the first, second, fifth, tenth, and fiftieth cycles. This sample shows a very high first-cycle discharge capacity of 1318 mA h g^{-1} and delivers a charge capacity of 837 mA h g^{-1}, giving rise to an irreversible capacity loss of approximately 36.5 %. The irreversible capacity loss may mainly be attributed to irreversible processes, such as the inevitable formation of an SEI film and electrolyte decomposition.[45,46] This is common for most anode materials. From the second cycle onwards, the coaxial Fe_3O_4@C hollow particles exhibit a very high capacity of over 904 mA h g^{-1}, with stable capacity retention of above 96.2 % after 50 cycles at a current density of 1 A g^{-1}.

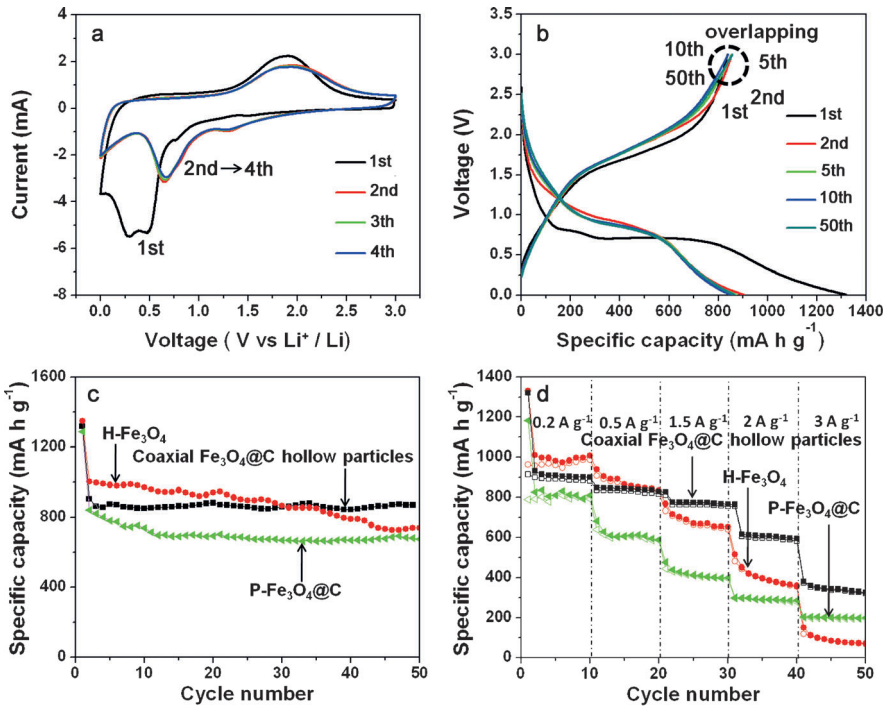

Figure 5. a) Cyclic voltammograms of coaxial Fe_3O_4@C hollow particles at a scan rate of 0.5 mV s^{-1} between 0.001 and 3.0 V, b) discharge–charge profiles of coaxial Fe_3O_4@C hollow particles for the initial 50 cycles at a current density of 1 A g^{-1}, c) discharge capacity versus cycle number plots of P-Fe_3O_4@C, H-Fe_3O_4, and coaxial Fe_3O_4@C hollow particles measured at a current density of 1 A g^{-1}, and d) the rate capability of P-Fe_3O_4@C, H-Fe_3O_4, and coaxial Fe_3O_4@C hollow particles at different current densities between 0.2 and 3 A g^{-1}.

Figure 5c shows the cycling performance of the Fe_2O_3 particles, P-Fe_3O_4, P-Fe_3O_4@C, H-Fe_3O_4, and coaxial Fe_3O_4@C hollow particles at a current density of 1 A g^{-1}. The capacity fade of H-Fe_3O_4 is rather severe and after 50 cycles is reduced to only 738.5 mA h g^{-1}. This is because of the poor electron conductivity and ion permeability of this semiconductor at a relatively high current density. As to the P-Fe_3O_4@C hybrid material, although its capacity fade is substantially less than that of H-Fe_3O_4, the initial capacity and the capacity of the 50th cycle (only 841 and 673.5 mA h g^{-1}, respectively) are relatively unsatisfactory. Remarkably, the coaxial Fe_3O_4@C hollow particles exhibit a high reversible capacity of 864 mA h g^{-1} after 50 cycles. More strikingly, the long cycle performance of the coaxial Fe_3O_4@C hollow particles is excellent after 150 cycles, also showing a reversible capacity as high as about 800 mA h g^{-1} (Figure S7 in the Supporting Information). Due to the lack of a protective carbon shell and a developed pore structure, P-Fe_3O_4 and Fe_2O_3 particles exhibit considerably inferior electrochemical performance, retaining capacities of 444 and 135 mA h g^{-1}, respectively, after 50 cycles (Figure S8a in the Supporting Information). The sample made with a reduced initial dopamine concentration (0.25 mg mL^{-1}) also displays inferior electrochemical performance (Figure S9 in the Supporting Information). It appears that the coaxial Fe_3O_4@C hollow particles demonstrate much better cyclic retention than the carbon-coated Fe_3O_4 hybrid material (P-Fe_3O_4@C) and hollow Fe_3O_4 (H-Fe_3O_4). The initial Coulombic efficiency of the coaxial Fe_3O_4@C hollow particles (64%) is slightly lower than that of the other Fe_3O_4-based samples (66 and 69%), which results from its higher specific surface area (Figure S10 in the Supporting Information). However, the Coulombic efficiencies sharply increase to >97% during the subsequent cycles and the difference in Coulombic efficiencies between the three samples becomes negligible. To further verify the good electrochemical performance, the rate capability of the five samples was evaluated at currents in the range of 0.2–3 A g^{-1} at a cut-off voltage between 0.001 and 3.0 V Li^+/Li, and the results are shown in Figure 5d and Figure S8b in the Supporting Information. The discharge capacity of the coaxial Fe_3O_4@C hollow particles remained at 883, 817, 755, and 582 mA h g^{-1} at current densities of 0.2, 0.5, 1.5, and 2 A g^{-1}, respectively. At a high current of 3 A g^{-1}, the anode can still deliver a stable capacity of about 320 mA h g^{-1}, indicating an excellent rate capability. In comparison with P-Fe_3O_4@C and H-Fe_3O_4, the coaxial Fe_3O_4@C hollow particles showed outstanding rate capability, especially at a current of above 1.5 A g^{-1}. The significantly improved electrochemical performance is attributed to the unique two-shell coaxial hollow structure, which ensures sufficient electrolyte/electrode contact area and shortened electron/ion transport channels to improve electron/ion conductivity, and also adequate void space and continuous carbon layers to accommodate volume change. To further prove the advantages of such structures in enhancing electrochemical performance, the spent coaxial Fe_3O_4@C hollow particles were examined by TEM (Figure S10 in the Supporting Information). It reveals that the hollow interior space of Fe_3O_4@C disappeared after 50 cycles, which was widely accepted due to the repeated expansion and shrinkage of Fe_3O_4 during charge/discharge processes. However, the rice-grain structure was well retained and uniform carbon layers were still coated on the surface of Fe_3O_4 particles, suggesting the robustness of the coaxial Fe_3O_4@C hollow particles.

Conclusion

We have established a new method for the fabrication of coaxial Fe_3O_4@C hollow particles with a penetrated mesochannel by confined nanospace pyrolysis for high-performance lithium ion battery electrodes. This hollow structure simultaneously incorporates several desirable design features, for example, continuous carbon coating, hollow interior space (i.e., penetrated

mesochannels), large specific surface areas and pore volumes, and thin Fe_3O_4 walls, leading to excellent electrochemical performance. Notably, the coaxially penetrated mesochannel structure has small open holes at the ends of the particles, which allow electrolyte access and thus facilitate the rapid diffusion of lithium ions from the electrolyte to the active materials. The mesochannels with a diameter of approximately 18 nm in the hybrid materials can accommodate the tension caused by the Li^+ insertion/extraction, and prevent the pulverization of the active materials. LIBs based on this novel functional material are low cost but high performance and this should accelerate their adoption in practical applications.

Experimental Section

Synthesis of rod-shaped β-FeOOH nanoparticles

β-FeOOH nanoparticles were prepared by hydrolysis of an aqueous solution of ferric chloride. Typically, $FeCl_3 \cdot 6H_2O$ (5 g) was dissolved in deionized water (250 mL) and stirred for 30 min. The solution was then added to a round-bottomed flask and heated at 80 °C under magnetic stirring for 12 h to obtain uniform β-FeOOH nanoparticles. The particles were isolated by centrifugation and washed with water.

Synthesis of coaxial Fe_3O_4@C particles and other iron oxide derivatives

β-FeOOH nanoparticles (140 mg) were dispersed in Tris buffer (pH ≈8.5; 100 mL) by ultrasonication for 30 min to form a suspension. Subsequently, dopamine (100 mg) was added to the mixture under stirring. The mixture was subjected to continuous magnetic stirring at 30 °C for 24 h. After that, the precipitate, that is, β-FeOOH@polydopamine, was collected by centrifugation, and then washed several times with deionized water. For the silica-coating layer,[47] β-FeOOH@polydopamine was stirred with ethanol and deionized water and mixed with an aqueous solution of ammonia. Subsequently, a solution of cetyltrimethyl ammonium bromide (CTAB: 0.4 g) was added to the mixture with vigorous stirring for 30 min. Tetraethyl orthosilicate (TEOS: 0.5 mL) was added with further stirring for 16 h at room temperature. The two-shell hybrid material (named β-FeOOH@polydopamine@SiO_2) was separated by centrifugation and then washed with deionized water, followed by drying at 50 °C in a box oven for 12 h. The desiccated sample was then heated in a quartz tube to 500 °C in an Ar atmosphere at a rate of 0.5 °C min^{-1} and kept at that temperature for 4 h. After pyrolysis, the rice-grain-shaped Fe_3O_4@C@SiO_2 hybrid material was obtained. Fe_3O_4@C@SiO_2 was immersed in NaOH (0.1 M) at 50 °C for 24 h to remove the silica shell. The resulting sample is named coaxial Fe_3O_4@C hollow particles.

For comparison purposes and to shed light on the effect of the confined environment on the pore development, β-FeOOH, β-FeOOH@polydopamine, and β-FeOOH@SiO_2 were prepared by using the same protocol and underwent the identical pyrolysis procedure. Accordingly, we synthesized Fe_2O_3 particles, a porous Fe_3O_4@C composite (P-Fe_3O_4@C), and a porous Fe_3O_4@SiO_2 hybrid. After removal of the silica in the Fe_3O_4@SiO_2 hybrid, we obtained porous Fe_3O_4 (P-Fe_3O_4). Finally, hollow Fe_3O_4 particles (H-Fe_3O_4) were obtained through calcination of the Fe_3O_4@C@SiO_2 hybrid at 500 °C for 4 h in air, followed by hydrogen-reduction and silica-removal procedures.

Characterization

Thermogravimetric analysis was performed from room temperature to 800 °C in air with a heating rate of 10 °C min^{-1} by using a STA449 F3 Jupiter thermogravimetric analyzer (NETZSCH). The X-ray diffraction (XRD) measurements were taken on a Rigaku D/Max 2400 diffractometer by using $Cu_{K\alpha}$ radiation (40 kV, 100 mA, $\lambda =$ 1.5406 Å). Nitrogen-adsorption isotherms were measured with a Micromeritics ASAP 2020 adsorption analyzer at 77.4 K. Before the measurements, all the samples were degassed at 200 °C for 6 h. The specific surface areas (S_{BET}) were calculated from the adsorption data in the relative pressure range of 0.05 to 0.3 by using the Brunauer–Emmett–Teller (BET) method. The total pore volume (V_{total}) was estimated from the amount adsorbed at a relative pressure of 0.90. Scanning electron microscopy (SEM) investigations were carried out with a Hitachi S-4800I instrument at 10 kV. Transmission electron microscopy (TEM) images were obtained with a FEI Tecnai F30 or a Hitachi HF2000 transmission electron microscope, equipped with a cold-field emission gun.

Electrochemical tests

Electrochemical experiments were performed through CR2025 coin-type test cells assembled in an argon-filled glovebox with lithium metal as the counter and reference electrodes at room temperature. The working electrodes were prepared by mixing the electrode material, carbon black, and poly(vinyldifluoride) (PVDF) at a weight ratio of 70:15:15, and pasted on a Cu foil. The electrode area was approximately 1.13 cm^2 and the loading of the active material was approximately 3.0 mg cm^{-2}. A Celgard 2400 membrane was used as a separator. The electrolyte consisted of a solution of $LiPF_6$ (1 M) in dimethyl carbonate (DMC), ethyl methyl carbonate (EMC), and ethylene carbonate (EC; 1:1:1 v/v/v). The discharge/charge measurements were carried out at several different current densities between cut off potentials of 0.001 and 3 V by using a Land CT2001A battery test system. The specific capacity of the coaxial Fe_3O_4@C nanocylinders and P-Fe_3O_4@C composite were calculated on the basis of the total mass of Fe_3O_4 and the carbon shell. Cyclic voltammogram (CV) measurements and electrochemical impedance spectra (EIS) were performed on a CHI660D electrochemical workstation.

Acknowledgements

The project was supported by the NSFC (No. 21073026) and the National Natural Science Funds for Distinguished Young Scholars (No. 21225312).

Keywords: carbon · electrodes · iron oxide · lithium · lithium-ion batteries · pyrolysis

[1] J. M. Tarascon, M. Armand, *Nature* **2001**, *414*, 359–367.
[2] Y. Idota, T. Kubota, A. Matsufuji, Y. Maekawa, T. Miyasaka, *Science* **1997**, *276*, 1395–1397.
[3] K. T. Nam, D. W. Kim, P. J. Yoo, C. Y. Chiang, N. Meethong, P. T. Hammond, Y. M. Chiang, A. M. Belcher, *Science* **2006**, *312*, 885–888.
[4] X. W. Lou, C. M. Li, L. A. Archer, *Adv. Mater.* **2009**, *21*, 2536–2539.
[5] Y. Ma, C. Zhang, G. Ji, J. Y. Lee, *J. Mater. Chem.* **2012**, *22*, 7845–7850.
[6] W. M. Zhang, X. L. Wu, J. S. Hu, Y. G. Guo, L. J. Wan, *Adv. Funct. Mater.* **2008**, *18*, 3941–3946.
[7] J. S. Zhou, H. H. Song, X. H. Chen, L. J. Zhi, S. B. Yang, J. P. Huo, W. T. Yang, *Chem. Mater.* **2009**, *21*, 2935–2940.

[8] Z. M. Cui, L. Y. Jiang, W. G. Song, Y. G. Guo, *Chem. Mater.* **2009**, *21*, 1162 – 1166.
[9] G. M. Zhou, D. W. Wang, F. Li, L. L. Zhang, N. Li, Z. S. Wu, L. Wen, G. Q. Lu, H. M. Cheng, *Chem. Mater.* **2010**, *22*, 5306 – 5313.
[10] M. Zhang, D. N. Lei, X. M. Yin, L. B. Chen, Q. H. Li, Y. G. Wang, T. H. Wang, *J. Mater. Chem.* **2010**, *20*, 5538 – 5543.
[11] Y. Z. Piao, H. S. Kim, Y. E. Sung, T. Hyeon, *Chem. Commun.* **2010**, *46*, 118 – 120.
[12] T. Yoon, C. Chae, Y.-K. Sun, X. Zhao, H. H. Kungc, J. K. Lee, *J. Mater. Chem.* **2011**, *21*, 17325 – 17330.
[13] W. Wei, S. B. Yang, H. X. Zhou, I. Lieberwirth, X. L. Feng, K. Müllen, *Adv. Mater.* **2013**, *25*, 2909 – 2914.
[14] E. Kang, Y. S. Jung, A. S. Cavanagh, G. H. Kim, S. M. George, A. C. Dillon, J. K. Kim, J. Lee, *Adv. Funct. Mater.* **2011**, *21*, 2430 – 2438.
[15] J. Kim, M. K. Chung, B. H. Ka, J. H. Ku, S. Park, J. Ryu, S. M. Oh, *J. Electrochem. Soc.* **2010**, *157*, A412 – A417.
[16] T. Zhu, J. S. Chen, X. W. Lou, *J. Phys. Chem. C* **2011**, *115*, 9814 – 9820.
[17] L. Li, T. Wang, L. Zhang, Z. Su, C. Wang, R. Wang, *Chem. Eur. J.* **2012**, *18*, 11417 – 11422.
[18] J. S. Chen, Y. M. Zhang, X. W. Lou, *ACS Appl. Mater. Interfaces* **2011**, *3*, 3276 – 3279.
[19] S. M. Yuan, J. X. Li, L. T. Yang, L. W. Su, L. Liu, Z. Zhou, *ACS Appl. Mater. Interfaces* **2011**, *3*, 705 – 709.
[20] T. Muraliganth, A. V. Murugan, A. Manthiram, *Chem. Commun.* **2009**, 7360 – 7362.
[21] Y. Wu, Y. Wei, J. Wang, K. Jiang, S. Fan, *Nano Lett.* **2013**, *13*, 818 – 823.
[22] Y. S. Jung, K. T. Lee, *Electrochim. Acta* **2007**, *52*, 7061 – 7067.
[23] J. E. Lee, S. H. Yu, D. J. Lee, D. C. Lee, S. I. Han, Y. E. Sung, T. Hyeon, *Energy Environ. Sci.* **2012**, *5*, 9528 – 9533.
[24] Z. Y. Wang, L. Zhou, X. W. Lou, *Adv. Mater.* **2012**, *24*, 1903 – 1911.
[25] Y. J. Hong, M. Y. Son, Y. C. Kang, *Adv. Mater.* **2013**, *25*, 2279 – 2283.
[26] H. Cheng, Z. G. Lu, R. G. Ma, Y. C. Dong, H. E. Wang, L. J. Xi, L. X. Zheng, C. K. Tsang, H. Li, C. Y. Chung, J. A. Zapien, Y. Y. Li, *J. Mater. Chem.* **2012**, *22*, 22692 – 22698.
[27] X. Y. Lai, J. E. Halpert, D. Wang, *Energy Environ. Sci.* **2012**, *5*, 5604 – 5618.
[28] F. B. Su, C. K. Poh, J. S. Chen, G. W. Xu, D. Wang, Q. Li, J. Y. Lin, X. W. Lou, *Energy Environ. Sci.* **2011**, *4*, 717 – 724.
[29] J. Y. Wang, N. L. Yang, H. J. Tang, Z. H. Dong, Q. Jin, M. Yang, D. Kisailus, H. J. Zhao, Z. Y. Tang, D. Wang, *Angew. Chem.* **2013**, *125*, 6545 – 6548; *Angew. Chem. Int. Ed.* **2013**, *52*, 6417 – 6420.
[30] Y. Z. Piao, J. Kim, H. B. Na, D. Kim, J. S. Baek, M. K. Ko, J. H. Lee, M. Shokouhimehr, T. Hyeon, *Nat. Mater.* **2008**, *7*, 242 – 247.
[31] H. Lee, S. M. Dellatore, W. M. Miller, P. B. Messersmith, *Science* **2007**, *318*, 426 – 430.
[32] R. Liu, S. M. Mahurin, C. Li, R. R. Unocic, J. C. Idrobo, H. J. Gao, S. J. Pennycook, S. Dai, *Angew. Chem.* **2011**, *123*, 6931 – 6934; *Angew. Chem. Int. Ed.* **2011**, *50*, 6799 – 6802.
[33] C. Lei, F. Han, D. Li, W. C. Li, Q. Sun, X. Q. Zhang, A. H. Lu, *Nanoscale* **2013**, *5*, 1168 – 1175.
[34] F. Cheng, K. L. Huang, S. Q. Liu, J. L. Liu, R. J. Deng, *Electrochim. Acta* **2011**, *56*, 5593 – 5598.
[35] C. He, S. Wu, N. Zhao, C. SHi, E. Liu, J. Li, *ACS Nano*, **2013**, *7*, 4459 – 4469.
[36] L. L. Wang, J. W. Liang, Y. C. Zhu, T. Mei, X. Zhang, Q. Yang, Y. T. Qian, *Nanoscale* **2013**, *5*, 3627 – 3631.
[37] M. W. Xu, L. B. Kong, W. J. Zhou, H. L. Li, *J. Phys. Chem. C* **2007**, *111*, 19141 – 19147.
[38] H. Jiang, L. P. Yang, C. Z. Li, C. Y. Yan, P. S. Lee, J. Ma, *Energy Environ. Sci.* **2011**, *4*, 1813 – 1819.
[39] Q. Sun, W. C. Li, A. H. Lu, *Small* **2013**, *9*, 2086 – 2090.
[40] X. Q. Zhang, Q. Sun, W. Dong, D. Li, A. H. Lu, J. Q. Mu, W. C. Li, *J. Mater. Chem. A* **2013**, *1*, 9449 – 9455.
[41] C. T. Hsieh, J. Y. Lin, C. Y. Mo, *Electrochim. Acta* **2011**, *58*, 119 – 124.
[42] X. J. Zhu, Y. W. Zhu, S. Murali, M. D. Stoller, R. S. Ruoff, *ACS Nano* **2011**, *5*, 3333 – 3338.
[43] H. J. Kim, K. I. Choi, A. Q. Pan, I. D. Kim, H. R. Kim, K. M. Kim, C. W. Na, G. Z. Cao, J. H. Lee, *J. Mater. Chem.* **2011**, *21*, 6549 – 6555.
[44] F. Han, D. Li, W. C. Li, C. Lei, Q. Sun, A. H. Lu, *Adv. Funct. Mater.* **2013**, *23*, 1692 – 1700.
[45] B. Jang, M. Park, O. B. Chae, S. Park, Y. Kim, S. M. Oh, Y. Piao, T. Hyeon, *J. Am. Chem. Soc.* **2012**, *134*, 15010 – 15015.
[46] Y. Gong, S. Yang, Z. Liu, L. Ma, R. Vajtai, P. M. Ajayan, *Adv. Mater.* **2013**, *25*, 3979 – 3984.
[47] A. H. Lu, T. Sun, W. C. Li, Q. Sun, F. Han, D. H. Liu, Y. Guo, *Angew. Chem.* **2011**, *123*, 11969 – 11972; *Angew. Chem. Int. Ed.* **2011**, *50*, 11765 – 11768.

Received: August 12, 2013
Published online on November 22, 2013